

# The rapidly evolving hypergiant IRC +10 420: High-resolution bispectrum speckle-interferometry and dust-shell modelling

T. Blöcker<sup>1</sup>, Y. Balega<sup>2</sup>, K.-H. Hofmann<sup>1</sup>, J. Lichtenthäler<sup>1</sup>, R. Osterbart<sup>1</sup>, and G. Weigelt<sup>1</sup>

<sup>1</sup> Max-Planck-Institut für Radioastronomie, Auf dem Hügel 69, D-53121 Bonn, Germany

<sup>2</sup> Special Astrophysical Observatory, Nizhnij Arkhyz, Zelenchuk region, 35147 Karachai-Cherkesia, Russia

Received 9 October 1998 / Accepted 4 June 1999

**Abstract.** The hypergiant IRC +10 420 is a unique object for the study of stellar evolution since it is the only object that is believed to be witnessed in its rapid transition from the red supergiant stage to the Wolf-Rayet phase. Its effective temperature has increased by 1000–2000 K within only 20 yr. We present the first speckle observations of IRC +10 420 with 73 mas resolution. A diffraction-limited  $2.11 \mu\text{m}$  image was reconstructed from 6 m telescope speckle data using the bispectrum speckle-interferometry method. The visibility function shows that the dust shell contributes  $\sim 40\%$  to the total flux and the unresolved central object  $\sim 60\%$ .

Radiative transfer calculations have been performed to model both the spectral energy distribution and visibility function. The grain sizes,  $a$ , were found to be in accordance with a standard distribution function,  $n(a) \sim a^{-3.5}$ , with  $a$  ranging between  $a_{\text{min}} = 0.005 \mu\text{m}$  and  $a_{\text{max}} = 0.45 \mu\text{m}$ . The observed dust shell properties cannot be fitted by single-shell models but seem to require multiple components. At a certain distance we considered an enhancement over the assumed  $1/r^x$  density distribution. The best model for *both* SED *and* visibility was found for a dust shell with a dust temperature of 1000 K at its inner radius of  $69 R_*$ . At a distance of  $308 R_*$  the density was enhanced by a factor of 40 and its density exponent was changed from  $x = 2$  to  $x = 1.7$ . The shell's intensity distribution was found to be ring-like. The ring diameter is equal to the inner diameter of the hot shell ( $\sim 69$  mas). The diameter of the central star is  $\sim 1$  mas. The assumption of a hotter inner shell of 1200 K gives fits of almost comparable quality but decreases the spatial extension of both shells' inner boundaries by  $\sim 30\%$  (with  $x = 1.5$  in the outer shell). The two-component model can be interpreted in terms of a termination of an enhanced mass-loss phase roughly 60 to 90 yr (for  $d = 5$  kpc) ago. The bolometric flux,  $F_{\text{bol}}$ , is  $8.17 \cdot 10^{-10} \text{ W m}^{-2}$  corresponding to a central-star luminosity of  $L/L_{\odot} = 25\,462 \cdot (d/\text{kpc})^2$ .

**Key words:** stars: Wolf-Rayet – stars: supergiants – stars: mass-loss – stars: individual: IRC +10 420 – stars: circumstellar matter – techniques: image processing

## 1. Introduction

The star IRC +10 420 (= V 1302 Aql = IRAS 19244+1115) is an outstanding object for the study of stellar evolution. Its spectral type changed from F8 I<sub>a</sub><sup>+</sup> in 1973 (Humphreys et al. 1973) to mid-A today (Oudmaijer et al. 1996, Klochkova et al. 1997) corresponding to an effective temperature increase of 1000–2000 K within only 20 yr. It is one of the brightest IRAS objects and one of the warmest stellar OH maser sources known (Giguere et al. 1976, see also Mutel et al. 1979, Diamond et al. 1983, Bowers 1984, Nedoluha & Bowers 1992). Ammonia emission has been reported by McLaren & Betz (1980) and Menten & Alcolea (1995). Large mass-loss rates, typically of the order of several  $10^{-4} M_{\odot}/\text{yr}$  (Knapp & Morris 1985, Oudmaijer et al. 1996) were determined by CO observations. Two evolutionary scenarios have been suggested for IRC +10 420: It is either a post-AGB (AGB: Asymptotic Giant Branch) star evolving through the proto-planetary nebula stage (e.g. Fix & Cobb 1987, Hrivnak et al. 1989, Bowers & Knapp 1989), or it is a massive hypergiant evolving from the RSG (Red Supergiant Branch) branch towards the Wolf-Rayet phase (e.g. Mutel et al. 1979, Nedoluha & Bowers 1992, Jones et al. 1993, Oudmaijer et al. 1996, Klochkova et al. 1997). However, due to its distance ( $d = 3\text{--}5$  kpc), large wind velocity ( $40 \text{ km s}^{-1}$ ) and photometric history, IRC +10 420 is most likely a luminous massive star (see Jones et al. 1993 and Oudmaijer et al. 1996), therefore being the only massive object observed until now in its transition to the Wolf-Rayet phase. The structure of the circumstellar environment of IRC +10 420 appears to be very complex (Humphreys et al. 1997), and scenarios proposed to explain the observed spectral features of IRC +10 420 include a rotating equatorial disk (Jones et al. 1993), bipolar outflows (Oudmaijer et al. 1994), and the infall of circumstellar material (Oudmaijer 1998).

Previous infrared speckle and coronagraphic observations were reported by Dyck et al. (1984), Ridgway et al. (1986), Cobb & Fix (1987), Christou et al. (1990) and Kastner & Weintraub (1995). In this paper we present diffraction-limited 73 mas bispectrum speckle-interferometry observations of the dust shell of IRC +10 420 as well as radiative transfer calculations to model its spectral energy distribution and visibility.

---

Send offprint requests to: T. Blöcker (bloecker@mpifr-bonn.mpg.de)

## 2. Observations and data reduction

The IRC +10 420 speckle interferograms were obtained with the Russian 6 m telescope at the Special Astrophysical Observatory on June 13 and 14, 1998. The speckle data were recorded with our NICMOS-3 speckle camera (HgCdTe array,  $256^2$  pixels, frame rate 2 frames/s) through an interference filter with a centre wavelength of  $2.11 \mu\text{m}$  and a bandwidth of  $0.19 \mu\text{m}$ . Speckle interferograms of the unresolved star HIP 95447 were taken for the compensation of the speckle interferometry transfer function. The observational parameters were as follows: exposure time/frame 50 ms; number of frames 8400 (5200 of IRC +10 420 and 3200 of HIP 95447);  $2.11 \mu\text{m}$  seeing (FWHM)  $\sim 1''.0$ ; field of view  $7''.8 \times 7''.8$ ; pixel size 30.5 mas. A diffraction-limited image of IRC +10 420 with 73 mas resolution was reconstructed from the speckle interferograms using the bispectrum speckle-interferometry method (Weigelt 1977, Lohmann et al. 1983, Hofmann & Weigelt 1986). The bispectrum of each frame consisted of  $\sim 37$  million elements. The modulus of the object Fourier transform (visibility) was determined with the speckle interferometry method (Labeyrie 1970).

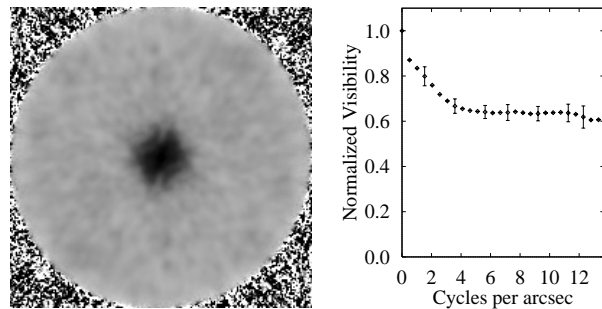
It is noteworthy that  $2.11 \mu\text{m}$  filters also serve to image hydrogen emission as, for instance,  $\text{H}_2$  ( $2.125 \mu\text{m}$ ) or  $\text{Br}\gamma$  ( $2.166 \mu\text{m}$ ) emission. Accordingly, it is possible that one might look at hydrogen emission rather than at the dust emission of a circumstellar shell. The low-resolution spectrum of IRC +10 420 published in the atlas of Hanson et al. (1996) shows a  $\text{Br}\gamma$  line in emission as the most prominent feature for the wavelength range considered here. Oudmaijer et al. (1994) carried out high-resolution infrared spectroscopy and found an equivalent width of  $1.2 \text{ \AA}$  for the  $\text{Br}\gamma$  emission line. This is only 0.06% of the bandwidth of our interference filter and consequently negligible.

Fig. 1 shows the reconstructed  $2.11 \mu\text{m}$  visibility function of IRC +10 420. There is only marginal evidence for an elliptical visibility shape (position angle of the long axis  $\sim 130^\circ \pm 20^\circ$ , axis ratio  $\sim 1.0$  to 1.1). The visibility 0.6 at frequencies  $> 4$  cycles/arcsec shows that the stellar contribution to the total flux is  $\sim 60\%$  and the dust shell contribution is  $\sim 40\%$ . In order to compare our results with speckle observations of other groups we determined the Gauß fit FWHM diameter of the dust shell to be  $d_{\text{FWHM}} = (219 \pm 30) \text{ mas}$ . By comparison, Christou et al. (1990) found for 3.8 m telescope K-band data a dust-shell flux contribution of  $\sim 50\%$  and  $d_{\text{FWHM}} = 216 \text{ mas}$ . However, as will be shown later, a ring-like intensity distribution appears to be much better suited than the assumption of a Gaussian distribution whose corresponding FWHM diameter fit may give misleading sizes (see Sect. 3.4.5). Fig. 2 displays the azimuthally averaged diffraction-limited images of IRC +10 420 and the unresolved star HIP 95447.

## 3. Dust shell models

### 3.1. Spectral energy distribution

The spectral energy distribution (SED) of IRC +10 420 with 9.7 and  $18 \mu\text{m}$  silicate emission features is shown in Fig. 3. It cor-



**Fig. 1.** *Left:* Two-dimensional  $2.11 \mu\text{m}$  visibility function of IRC +10 420 shown up to the diffraction limit (see right panel). The dark central structure shows that the central object is surrounded by a dust shell. *Right:* Azimuthally averaged  $2.11 \mu\text{m}$  visibility of IRC +10 420 with error bars for selected frequencies. This visibility function consists of a constant plateau (visibility  $\sim 0.6$ ) caused by the unresolved central object and a triangle-shaped low-frequency function caused by the faint extended nebula.

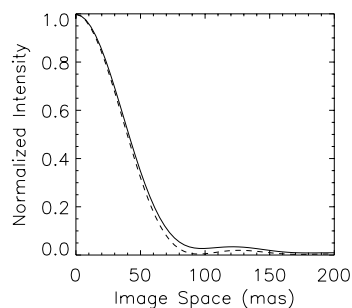


**Fig. 2.** Azimuthally averaged radial plots of the reconstructed diffraction-limited  $2.11 \mu\text{m}$ -images of IRC +10 420 (solid line) and HIP 95447 (dashed line).

responds to the ‘1992’ data set used by Oudmaijer et al. (1996) and combines VRI (October 1991), near-infrared (March and April 1992) and Kuiper Airborne Observatory photometry (June 1991) of Jones et al. (1993) with the IRAS measurements and 1.3 mm data from Walmsley et al. (1991). Additionally, we included the data of Craine et al. (1976) for  $\lambda < 0.55 \mu\text{m}$ . In contrast to the near-infrared, the optical magnitudes have remained constant during the last twenty years within a tolerance of  $\approx 0^{\text{m}}1$ .

IRC +10 420 is highly reddened due to an extinction of  $A_{\text{V}}^{\text{total}} \approx 7^{\text{m}}$  by the interstellar medium and the circumstellar shell. From polarization studies Craine et al. (1976) estimated an interstellar extinction of  $A_{\text{V}} \approx 6^{\text{m}}$ . Jones et al. (1993) derived from their polarization data  $A_{\text{V}} \approx 6^{\text{m}}$  to  $7^{\text{m}}$ . Based on the strength of the diffuse interstellar bands Oudmaijer (1998) inferred  $E(B - V) = 1^{\text{m}}4 \pm 0^{\text{m}}5$  for the interstellar contribution compared to a total of  $E(B - V) = 2^{\text{m}}4$ . We will use an interstellar  $A_{\text{V}}$  of  $5^{\text{m}}$  as in Oudmaijer et al. (1996). This interstellar reddening was taken into account by adopting the method of Savage & Mathis (1979) with  $A_{\text{V}} = 3.1E(B - V)$ .

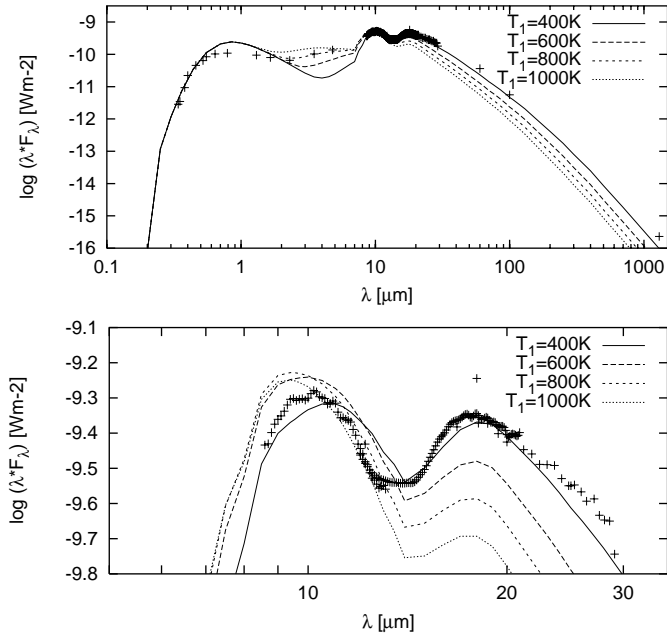


**Fig. 3.** Model SED for  $T_{\text{eff}} = 7000$  K,  $\tau_{0.55 \mu\text{m}} = 5$  and different dust temperatures  $T_1$ . The lower panel shows the silicate features. The calculations are based on a black body, Draine & Lee (1984) silicates, and an MRN grain size distribution with  $a_{\text{max}} = 0.2 \mu\text{m}$ . The symbols (+) refer to the observations (see text) corrected for interstellar extinction of  $A_v = 5^m$ .

### 3.2. The radiative transfer code

In order to model both the observed SED and  $2.11 \mu\text{m}$  visibility, we performed radiative transfer calculations for dust shells assuming spherical symmetry. We used the code DUSTY developed by Ivezić et al. (1997), which solves the spherical radiative transfer problem utilizing the self-similarity and scaling behaviour of IR emission from radiatively heated dust (Ivezić & Elitzur 1997). To solve the radiative transfer problem including absorption, emission and scattering several properties of the central source and its surrounding envelope are required, viz. (i) the spectral shape of the central source’s radiation; (ii) the dust properties, i.e. the envelope’s chemical composition and grain size distribution as well as the dust temperature at the inner boundary; (iii) the relative thickness of the envelope, i.e. the ratio of outer to inner shell radius, and the density distribution; and (iv) the total optical depth at a given reference wavelength. The code has been expanded for the calculation of synthetic visibilities as described by Gauger et al. (1999).

### 3.3. Single-shell models

We calculated various models considering the following parameters within the radiative transfer calculations: SED and visibility were modelled for  $T_{\text{eff}} = 7000$  to  $9000$  K, black bodies and Kurucz (1992) model atmospheres as central sources of radiation, different silicates (Draine & Lee 1984, Ossenkopf et al. 1992, David & Pegourie 1995), single-sized grains with  $a = 0.01$  to  $0.6 \mu\text{m}$  and grain size distributions according to

Mathis et al. (1977, hereafter MRN), i.e.  $n(a) \sim a^{-3.5}$ , with  $0.005 \mu\text{m} \leq a \leq (0.20 \text{ to } 0.60) \mu\text{m}$ . We used a  $1/r^2$  density distribution and a shell thickness  $Y_{\text{out}} = r_{\text{out}}/r_1$  of  $10^3$  to  $10^5$  with  $r_{\text{out}}$  and  $r_1$  being the outer and inner radius of the shell, respectively. Then, the remaining fit parameters are the dust temperature,  $T_1$ , which determines the radius of the shell’s inner boundary,  $r_1$ , and the optical depth,  $\tau$ , at a given reference wavelength,  $\lambda_{\text{ref}}$ . We refer to  $\lambda_{\text{ref}} = 0.55 \mu\text{m}$ . Models were calculated for dust temperatures between 400 and 1000 K and optical depths between 1 and 12. Significantly larger values for  $\tau$  lead to silicate features in absorption.

Fig. 3 shows the SED calculated for  $T_{\text{eff}}=7000$  K,  $Y_{\text{out}}=10^3$ , Draine & Lee (1984) silicates, MRN grain size distribution ( $a_{\text{max}} = 0.2 \mu\text{m}$ ) and different dust temperatures. It illustrates that the long-wavelength range is sufficiently well fitted for cool dust with  $T_1 = 400$  K, optical wavelengths and silicate features require  $\tau \sim 5$ . The inner radius of the dust shell is at  $r_1 = 447 R_*$  ( $R_*$ : stellar radius), the equilibrium temperature at the outer boundary amounts to  $T_{\text{out}} = 22$  K. However, the fit fails in the near-infrared underestimating the flux between 2 and  $5 \mu\text{m}$ . Instead this part of the SED seems to require much hotter dust of  $T_1 \gtrsim 800$  K ( $r_1 \lesssim 145 R_*$ ,  $T_{\text{out}} = 32$  K). This confirms the findings of Oudmaijer et al. (1996) who conducted radiative transfer calculations in the small particle limit, where scattering is negligible. They introduced a cool (400 K) and a hot (1000 K) shell to achieve an overall fit.

We found this behaviour of single-shell SEDs to be almost independent of various input parameters. Increasing  $Y_{\text{out}}$  from  $10^3$  to  $10^5$  leads to somewhat higher fluxes, but only for  $\lambda > 100 \mu\text{m}$ . The equilibrium temperature at the outer boundary decreases by a factor of two if the shell’s thickness is increased by one order of magnitude. Larger  $T_{\text{eff}}$  gives slightly less flux in the near-infrared, larger wavelengths ( $\lambda > 10 \mu\text{m}$ ) are almost unaffected. The Draine & Lee (1984) and David & Pegourie (1995) silicates give almost identical results, the optical constants of Ossenkopf et al. (1992) lead to a larger  $9.7 \mu\text{m}/18 \mu\text{m}$  flux ratio for the silicate features, to somewhat higher fluxes between 2 and  $10 \mu\text{m}$  and to a somewhat flatter slope of the SED at short wavelengths. However, the need for two dust components still exists. Calculations with different grain sizes show that single-sized grains larger than  $0.2 \mu\text{m}$  are not suitable for IRC +10 420. The silicate features are worse fitted and, in particular, a significant flux deficit appears in the optical and near-infrared. The variation of the maximum grain size in the MRN distribution leads to much smaller differences due to the steep decrease of the grain number density with grain size.

The  $2.11 \mu\text{m}$  visibility is very sensitive against scattering, thus depending strongly on the assumed grain sizes (see Groenewegen 1997) as demonstrated in Fig. 4. For a given set of parameters both *inclination* and *curvature* of the visibility are mainly given by the optical depth,  $\tau$ , and the grain size,  $a$ . Since  $\tau$  is fixed to small values due to the emission profiles,  $a$  can be determined. The dust temperature must be varied simultaneously since an increase of  $T_1$  leads to a steeper declining visibility. Our calculations show that the *visibility* is best fitted for an intermediate  $T_1 = 600$  K in contrast to the SED. Either single-

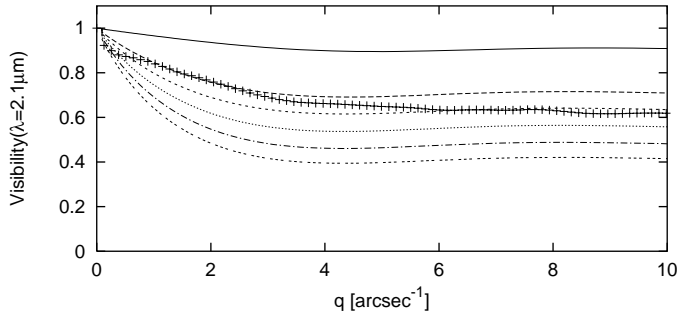


**Fig. 4.** Model visibility function for  $T_{\text{eff}} = 7000$  K,  $\tau_{0.55 \mu\text{m}} = 5$ ,  $T_1 = 600$  K and different maximum grain sizes in the MRN grain size distribution ( $a_{\text{max}} = 0.2, 0.4, 0.45, 0.5, 0.55$  and  $0.6 \mu\text{m}$  from top to bottom). The calculations are based on a black body and Draine & Lee (1984) silicates.

sized grains with  $a \sim 0.4 \mu\text{m}$  (which, however, are ruled out by the SED) or MRN grain size distributions with  $a_{\text{max}} \sim 0.45$  to  $0.5 \mu\text{m}$  are appropriate. This result still depends on the kind of silicates considered, i.e. on the optical constants. For instance, if we take the ‘warm silicates’ of Ossenkopf et al. (1992), we get somewhat smaller particles (by  $\sim 0.1 \mu\text{m}$ , i.e.  $a \sim 0.3 \mu\text{m}$  for single-sized grains and  $a_{\text{max}} \sim 0.35 \mu\text{m}$  for a grain distribution, resp.). The differences to the corresponding ‘cold silicates’ or to the data from David & Pegourie (1994) are found to be smaller. The fits to the SED are of comparable quality. We chose Draine & Lee (1984) silicates with  $a_{\text{min}} = 0.005 \mu\text{m}$  and  $a_{\text{max}} = 0.45 \mu\text{m}$ .

### 3.4. Multiple dust-shell components

#### 3.4.1. Two component shells

Since we failed to model the SED with the assumptions made so far, we introduced a two-component shell as Oudmaijer et al. (1996). For that purpose, we assume that IRC +10420 had passed through a superwind phase in its history as can be expected from its evolutionary status (see Schaller et al. 1992, García-Segura et al. 1996). This is in line with the conclusions drawn from the Oudmaijer et al. (1996) model and recent interpretations of HST data (Humphreys et al. 1997). A previous superwind phase leads to changes in the density distribution, i.e. there is a region in the dust shell which shows a density enhancement over the normal  $1/r^2$  distribution. The radial density distribution may also change within this superwind shell. For more details, see Suh & Jones (1997). Since dust formation operates on very short timescales in OH/IR stars, we assume a constant outflow velocity for most of the superwind phase and thus a  $1/r^2$  density distribution. For simplicity, we consider only single jumps with enhancement factors, or amplitudes,  $A$  at radii  $Y = r/r_1$  in the relative density distribution as demonstrated in Fig. 5.

Concerning the grains we stay with Draine & Lee (1984) silicates and an MRN grain size distribution with  $a_{\text{min}} = 0.005 \mu\text{m}$  and  $a_{\text{max}} = 0.45 \mu\text{m}$  as in the case of the single shell models.

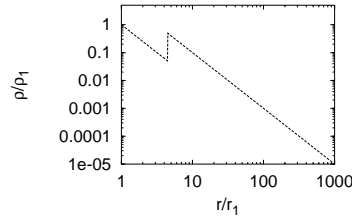


**Fig. 5.** Relative density distribution for a superwind at  $Y = r/r_1 = 4.5$  with an amplitude of  $A = 10$ .

The influence of different grain-size distributions will be discussed later.

We calculated a grid of models for  $T_1 = 1000$  K with superwinds at  $Y = 2.5$  to  $8.5$  with amplitudes  $A$  ranging from 10 to 80. Due to the introduced density discontinuity the flux conservation has to be controlled carefully, in particular at larger optical depths and amplitudes. SED and visibility behave contrarily concerning the adjustment of the superwind: The SED requires sufficiently large distances,  $Y \gtrsim 4.5$ , and moderate amplitudes,  $A \lesssim 20$  to  $40$ , in particular for the flux between  $2$  and  $10 \mu\text{m}$  and for  $\lambda > 20 \mu\text{m}$ . A good fit was found for  $Y = 6.5$  and  $A = 20$  corresponding to  $r_1 = 81 R_*$ . Note that the bolometric flux at the inner dust-shell radius (and therefore  $r_1/r_*$ ) is fully determined by the solution of the radiative transfer problem even though the overall luminosity is not (Ivezić & Elitzur 1997). The dust temperature at the density enhancement ( $r_2 = 527 R_*$ ) has dropped to  $322$  K. This agrees well with the model of Oudmaijer et al. (1996). The visibility, however, behaves differently. In order to reproduce the unresolved component (the plateau) large amplitudes,  $A \gtrsim 40$  to  $80$ , are required. On the other hand, the slope at low spatial frequencies is best reproduced for a close superwind shell,  $Y < 4.5$  (at this distance independent on  $A$ ). The best model found for *both* SED *and* visibility is that with  $Y = 4.5$  and  $A = 40$  as shown in Fig. 6. It corresponds to  $r_1 = 71 R_*$  and  $r_2 = 320 R_*$  (with  $T_2 \sim 475$  K), i.e. to angular diameters of  $\Theta_1 = 71$  mas and  $\Theta_2 = 321$  mas. The angular diameters depend on the model’s bolometric flux,  $F_{\text{bol}}$ , which is  $8.17 \cdot 10^{-10} \text{ W m}^{-2}$ . Accordingly, the central star has a luminosity of  $L/L_\odot = 25462 \cdot (d/\text{kpc})^2$  and an angular diameter of  $\Theta_* = 1.74 \cdot 10^9 \sqrt{F_{\text{bol}}/T_{\text{eff}}^4} \sim 1$  mas. Assuming a constant outflow velocity of  $v = 40 \text{ km s}^{-1}$ , the expansion ages of the two components are  $t_1/\text{yr} = 4.2 \cdot (d/\text{kpc})$  and  $t_2/\text{yr} = 18.9 \cdot (d/\text{kpc})$ . With a dust-to-gas ratio of  $0.005$  and a specific dust density of  $3 \text{ g cm}^{-3}$  the mass-loss rates of the components are  $\dot{M}_1 = 1.4 \cdot 10^{-5} M_\odot/\text{yr} \cdot (d/\text{kpc})$  and  $\dot{M}_2 = 5.5 \cdot 10^{-4} M_\odot/\text{yr} \cdot (d/\text{kpc})$ .

Fig. 7 shows the fractional contributions of the direct stellar radiation, the scattered radiation and the dust emission to the total emerging flux. The stellar contribution has its maximum at  $2.2 \mu\text{m}$  where it contributes  $60.4\%$  to the total flux in accordance with the observed visibility plateau of  $0.6$ . At this wavelength scattered radiation and dust emission amount to  $25.6\%$  and  $14\%$  of the total flux, respectively. Accordingly,  $64.6\%$  of the  $2.11 \mu\text{m}$  dust-shell emission is due to scattered stellar light and  $35.3\%$  due to direct thermal emission from dust. For  $\lambda \lesssim 1 \mu\text{m}$  the flux

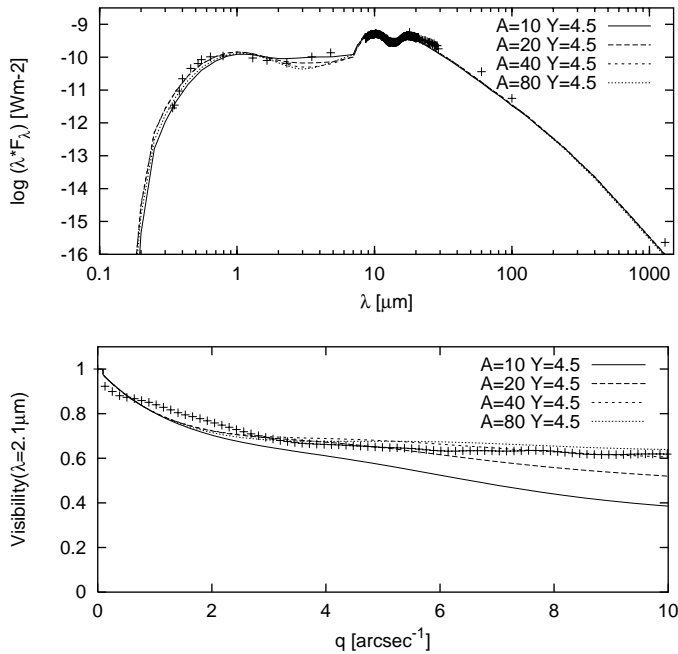


**Fig. 6.** SED (top) and visibility (bottom) for a superwind model with  $Y = r/r_1 = 4.5$  and different amplitudes. Model parameters are: black body,  $T_{\text{eff}} = 7000$  K,  $T_1 = 1000$  K,  $\tau_{0.55 \mu\text{m}} = 7.0$ , Draine & Lee (1984) silicates, Mathis et al. (1977) grain size distribution with  $a_{\text{max}} = 0.45 \mu\text{m}$ , and  $Y_{\text{out}} = 10^4$ . The symbols refer to the observations (see text) corrected for interstellar extinction of  $A_v = 5^m$ .

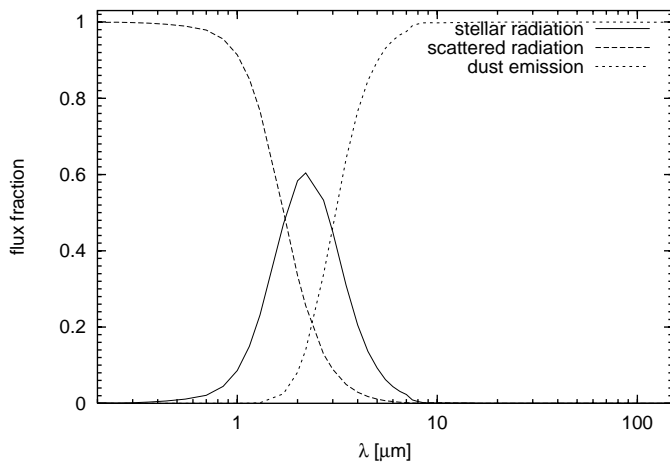


**Fig. 7.** Fractional contributions of the emerging stellar radiation as well as of the scattered radiation and of the dust emission to the total flux as a function of the wavelength for a superwind model with  $Y = r/r_1 = 4.5$  and  $A = 40$ . Model parameters are: black body,  $T_{\text{eff}} = 7000$  K,  $T_1 = 1000$  K,  $\tau_{0.55 \mu\text{m}} = 7.0$ , Draine & Lee (1984) silicates, Mathis et al. (1977) grain size distribution with  $a_{\text{max}} = 0.45 \mu\text{m}$ .

is determined by scattered radiation whereas for  $\lambda \gtrsim 10 \mu\text{m}$  dust emission dominates completely.

### 3.4.2. Influence of the grain-size distribution

As in the case of the single-shell models we also studied other grain size distributions. The MRN distribution derived for the

interstellar medium gives a continuous decrease of the number density with increasing grain sizes. On the other hand, the distribution of grains in dust-shells of evolved stars rather appears to be peaked at a dominant size (e.g. Krüger & Sedlmayr 1997, Winters et al. 1997). It is noteworthy that even in the case of a sharply peaked size distribution the few larger particles can contribute significantly to the absorption and scattering coefficients (see Winters et al. 1997). Accordingly, the  $2.11 \mu\text{m}$  visibility reacts sensitively if some larger particles are added whereas the SED does not, as demonstrated in the previous section. In order to study the influence of different grain size distributions on the two-component model we calculated grids of models with  $n(a) \sim a^q$  for different exponents ( $q = -3.0$  to  $-5.5$ ) and lower and upper cut-offs ( $a_{\text{min}} = 0.005$  to  $0.05 \mu\text{m}$  and  $a_{\text{max}} = 0.1$  to  $0.8 \mu\text{m}$ ). Additionally we considered single-sized grains ( $a = 0.1$  to  $0.8 \mu\text{m}$ ).

Concerning the visibility, a larger (smaller) negative exponent in the distribution function can, in principle, be compensated by increasing (decreasing) the maximum grain size. For instance,  $q = -4.0$  requires  $a_{\text{max}} = 0.55 \mu\text{m}$  to fit the  $2.11 \mu\text{m}$  visibility. On the other hand, if the distribution becomes too narrow, the SED cannot be fitted any longer since the  $9.7 \mu\text{m}$  silicate feature turns into absorption. A distribution with  $q = -3.8$  and  $a_{\text{max}} = 0.50 \mu\text{m}$  best reproduces the flux-peak ratio of the silicate features.

For a given exponent in the grain-size distribution function of  $q = -3.5$  we arrive at the same maximum grain size as in the case of the one-component model, viz.  $0.45 \mu\text{m}$ , in order to yield a fit for both the SED and the visibility (see Fig. 8). This is due to the fact that larger particles increase the curvature of the visibility curve at low spatial frequencies whereas the high-frequency tail (the plateau) is found at lower visibility values. On the other hand, the inclusion of some larger particles does not change the shape of the SED as discussed above.

If sufficiently small, the lower cut-off grain size can be changed moderately (within a factor of two) without any significant change for SED and visibility. If  $a_{\text{min}}$  exceeds, say,  $0.05 \mu\text{m}$ , the fits of the observations begin to become worse. For instance, the curvature of the visibility at low spatial frequencies and the flux-peak ratio of the silicate features are then overestimated.

Finally, we repeated the calculations under the assumption of single-sized grains. In order to model the visibility a grain size  $a$  close to  $0.3 \mu\text{m}$  is required as shown in Fig. 9. In contrast, the reproduction of the relative strengths of the silicate features seems to require smaller grains, viz. close to  $0.1 \mu\text{m}$ . Consequently, for the modelling of IRC +10420 a grain size distribution appears to be much better suited than single-sized grains.

### 3.4.3. Influence of the density distribution

Inspection of the best fits derived so far reveals that there are still some shortcomings of the models. First, although being within the observational error bars, the model visibilities always show a larger curvature at low spatial frequencies. This seems to be

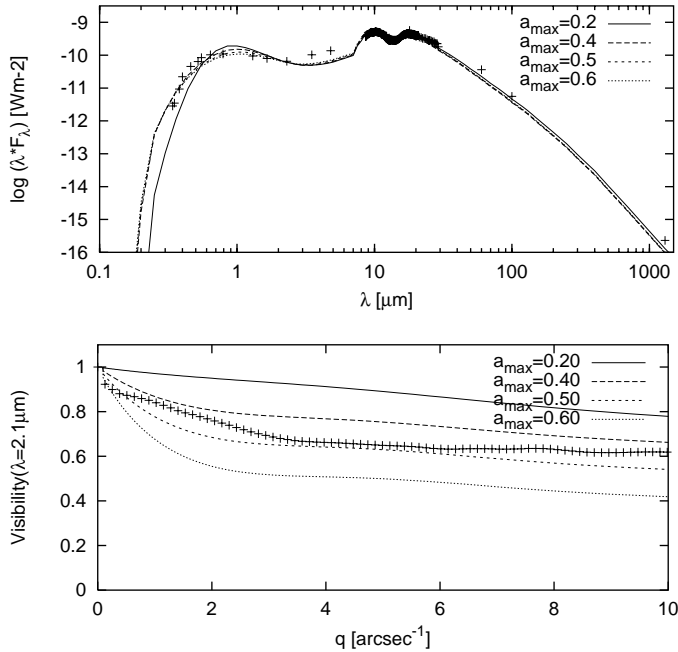


**Fig. 8.** SED (top) and visibility (bottom) for a superwind model with  $Y = r/r_1 = 4.5$  and  $A = 40$  calculated for Mathis et al. (1977) grain size distributions with  $a_{\max} = 0.20, 0.4, 0.5$  and  $0.6 \mu\text{m}$ . Model parameters are: black body,  $T_{\text{eff}} = 7000 \text{ K}$ ,  $T_1 = 1000 \text{ K}$ ,  $\tau_{0.55 \mu\text{m}} = 7.3$ , Draine & Lee (1984) silicates, and  $Y_{\text{out}} = 10^4$ . The symbols refer to the observations (see text) corrected for interstellar extinction of  $A_v = 5^m$ .

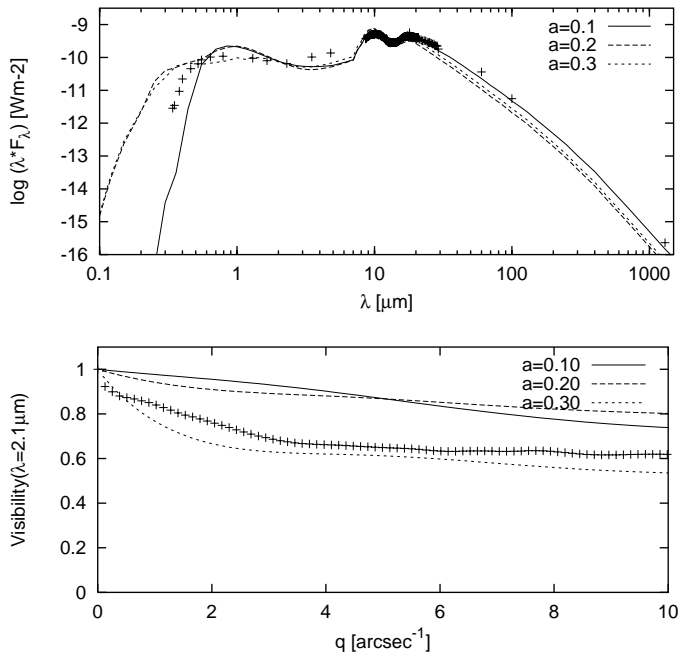


**Fig. 9.** SED (top) and visibility (bottom) for a superwind model with  $Y = r/r_1 = 4.5$  and  $A = 40$  for single-sized grains with  $a = 0.1, 0.2$  and  $0.3 \mu\text{m}$ . Model parameters are: black body,  $T_{\text{eff}} = 7000 \text{ K}$ ,  $T_1 = 1000 \text{ K}$ ,  $\tau_{0.55 \mu\text{m}} = 7.3$ , Draine & Lee (1984) silicates, and  $Y_{\text{out}} = 10^4$ . The symbols refer to the observations (see text) corrected for interstellar extinction of  $A_v = 5^m$ .

almost independent of the chosen grain-size distribution. Second, the flux beyond  $20 \mu\text{m}$  is somewhat too low. This may be due to our choice of a  $1/r^2$  density distribution for both shells. We recalculated the model grid for different  $1/r^x$  density distributions for both shells with  $x$  ranging between 1 and 4. A flatter distribution in the outer shell increases the flux in the long-wavelength range as required but leads also to a drop of the flux in the near-infrared. The plateau in the visibility curve remains unaffected but the curvature at low spatial frequencies is increased. To take advantage of the better far-infrared properties of cool shells with flatter density distributions, but to counteract their disadvantage in the near-infrared and at low spatial frequencies, the density distribution of the inner shell also has to be changed. It should be somewhat steeper than the normal  $1/r^2$  distribution. Then the near-infrared flux is raised and the visibility shows a smaller curvature in the low-frequency range. It should be noted that the curvature is most affected for superwinds of low amplitudes. However, the steeper density decrease in the inner shell leads to increasingly low visibility values in the high frequency range. Since this has to be compensated by an increase of the superwind amplitude the advantages of the steeper distribution are almost cancelled.

Thus, we can stay with a  $1/r^2$  density distribution in the inner shell and moderate superwind amplitudes ( $A \sim 40$ ). The then best suited models we found are those with superwinds at  $Y = 4.5$  and a  $1/r^{1.7}$  distribution in the outer shell. The corresponding SED and visibility are shown in Fig. 10 for different superwind amplitudes. We note again that the quality of the fits is in particular determined by the outer shell, whereas the inner shell's exponent is less constrained. A  $1/r^3$  distribution in the inner shell and large superwind amplitudes ( $A \gtrsim 80$ ) give similar results.

The radii of the inner and outer shell are  $r_1 = 69 R_*$  and  $r_2 = 308 R_*$  (with  $T_2 \sim 483 \text{ K}$ ), resp., corresponding to angular diameters of  $\Theta_1 = 69 \text{ mas}$  and  $\Theta_2 = 311 \text{ mas}$ . Adopting the same assumptions for outflow velocity, dust-to-gas ratio and specific dust density as in the previous section, the expansion ages are  $t_1/\text{yr} = 4.1 \cdot (d/\text{kpc})$  and  $t_2/\text{yr} = 18.4 \cdot (d/\text{kpc})$ , for the mass-loss rate of the inner component one gets  $\dot{M}_1 = 1.35 \cdot 10^{-5} M_\odot/\text{yr} \cdot (d/\text{kpc})$ . In the outer component either the outflow velocity has increased or the mass-loss rate has decreased with time due to the more shallow density distribution. Provided the outflow velocity has kept constant, the mass-loss rate at the end of the superwind phase, 92 yr ago, was  $\dot{M}_2 = 5.4 \cdot 10^{-4} M_\odot/\text{yr} \cdot (d/\text{kpc})$ , and, for instance, amounted to  $\dot{M}_2 = 8.0 \cdot 10^{-4} M_\odot/\text{yr} \cdot (d/\text{kpc})$  200 yr ago.

Since the flatter density distribution provides a better fit for the long-wavelength range of the SED, while the visibility is equally well fitted compared to the standard density distribution, it is superior to the model of Sect. 3.4.1. Fig. 11 gives the fractional flux contributions (stellar, dust, scattering) for the same model as shown in Fig. 7 but with an  $1/r^{1.7}$  distribution in the outer shell. The various flux contributions at  $2.11 \mu\text{m}$  are very similar to those of the  $1/r^2$  model: 62.2% stellar light, 26.1% scattered radiation and 10.7% dust emission. Thus, the total

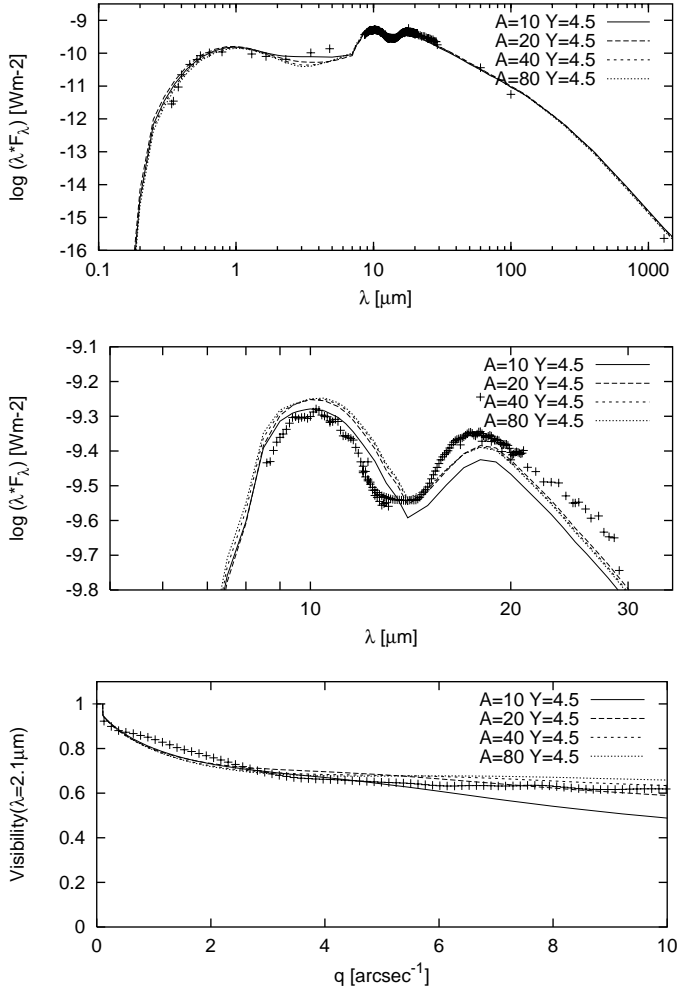


**Fig. 10.** SED (top), silicate features (middle) and visibility (bottom) for a superwind model with  $Y = r/r_1 = 4.5$  and different amplitudes. The inner shell obeys a  $1/r^2$  density distribution, the outer shell a  $1/r^{1.7}$  density distribution. Model parameters are: black body,  $T_{\text{eff}} = 7000$  K,  $T_1 = 1000$  K,  $\tau_{0.55 \mu\text{m}} = 7.0$ , Draine & Lee (1984) silicates, Mathis et al. (1977) grain size distribution with  $a_{\text{max}} = 0.45 \mu\text{m}$ , and  $Y_{\text{out}} = 10^4$ . The symbols refer to the observations (see text) corrected for interstellar extinction of  $A_v = 5^m$ .

emission of the circumstellar shell is composed of 70.9% scattered stellar light and 29.1% direct thermal emission from dust.

#### 3.4.4. Influence of the dust temperature

Finally, we studied the influence of the dust temperature at the inner boundary of the hot shell. For that purpose we recalculated the previous model grids for dust temperatures of 800 and 1200 K. As already shown for the single-shell models, an increase of the temperature at the inner boundary increases the flux in the near-infrared and substantially lowers the flux in the long-wavelength range. On the other hand, the higher the temperature the less is the curvature of the visibility at low spatial frequencies, the plateau is only significantly affected for low-amplitude superwinds. The shape of SED and  $2.11 \mu\text{m}$  visibility for different dust temperatures at the hot shell's inner boundary

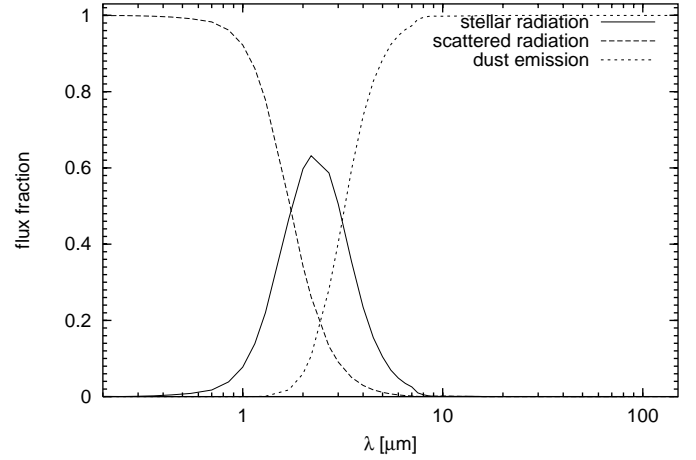


**Fig. 11.** Fractional contributions of the emerging stellar radiation as well as of the scattered radiation and of the dust emission to the total flux as a function of the wavelength for a superwind model with  $Y = r/r_1 = 4.5$ ,  $A = 40$  and a  $1/r^{1.7}$  density distribution in the outer shell. Model parameters are: black body,  $T_{\text{eff}} = 7000$  K,  $T_1 = 1000$  K,  $\tau_{0.55 \mu\text{m}} = 7.0$ , Draine & Lee (1984) silicates, Mathis et al. (1977) grain size distribution with  $a_{\text{max}} = 0.45 \mu\text{m}$ .

for a given superwind is demonstrated in Fig. 12. A temperature less than 1000 K can be excluded in particular due to the worse fit of the visibility for low frequencies. Instead, the 1200 K model gives a much better fit to the visibility than previous ones. Fig. 12 refers to an amplitude of  $A = 40$  in order to be directly comparable with the models shown before. We note that we get an even better fit assuming  $A = 80$ , which leaves the low-frequency-range unchanged but improves the agreement with the measured plateau.

However, the improvement of the  $2.11 \mu\text{m}$  visibility model due to a hotter inner shell with  $T_1 = 1200$  K is at the expense of a considerable amplification of the flux deficit for  $\lambda \gtrsim 20 \mu\text{m}$  in the SED. In order to compensate this effect we have had to assume a flatter density profile for the outer shell than in the case of the  $T_1 = 1000$  K., viz.  $\sim 1/r^{1.5}$  instead of  $\sim 1/r^{1.7}$ . The corresponding curves are shown in Fig. 13. Again, increasing the far-infrared fluxes, as required to model the SED, leads to an increase of the  $2.11 \mu\text{m}$  visibility's curvature at low spatial frequencies giving somewhat worse fits for the visibility. We note that the peak-ratio of the silicate features is better matched with a lower dust temperature of  $T_1 = 1000$  K.

The radii of the inner and outer shell are now considerably smaller than those of the previous models due to the higher temperature of the hot shell. The radiative transfer calculations give here  $r_1 = 47 R_*$  and  $r_2 = 210 R_*$  (with  $T_2 \sim 594$  K), resp., resulting in angular diameters of  $\Theta_1 = 47 \text{ mas}$  and  $\Theta_2 = 212 \text{ mas}$ . Accordingly, the expansion ages are  $t_1/\text{yr} = 2.8 \cdot (d/\text{kpc})$  and  $t_2/\text{yr} = 12.6 \cdot (d/\text{kpc})$ , for the mass-loss rate of the inner component one gets  $\dot{M}_1 = 9.2 \cdot 10^{-6} M_\odot/\text{yr} \cdot (d/\text{kpc})$ . Provided the outflow velocity has kept constant, the mass-loss rate at end of the superwind phase, 63 yr ago, was  $\dot{M}_2 = 3.7 \cdot 10^{-4} M_\odot/\text{yr} \cdot (d/\text{kpc})$ , and, for instance, amounted to  $\dot{M}_2 = 5.4 \cdot 10^{-4} M_\odot/\text{yr} \cdot (d/\text{kpc})$  200 yr ago.

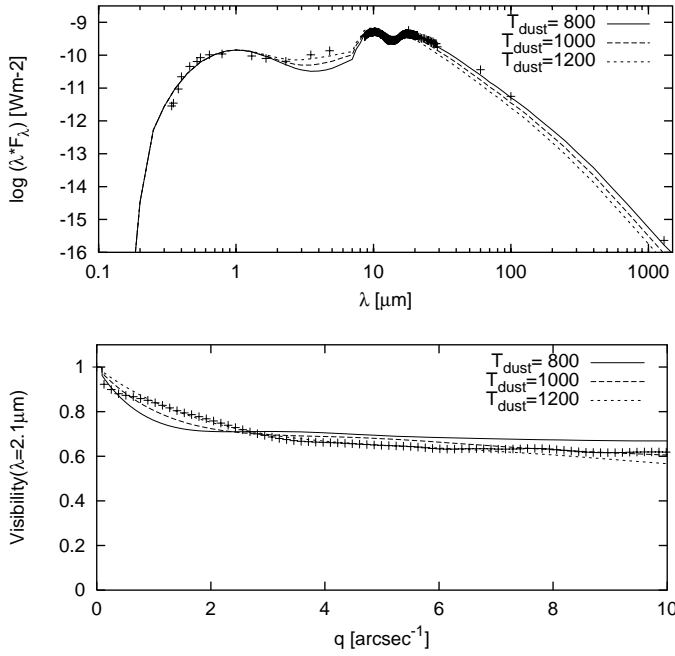


**Fig. 12.** SED (top) and visibility (bottom) for a superwind model ( $Y = r/r_1 = 4.5$  and  $A = 40$ ) with different temperatures for the inner boundary of the hot shell. Model parameters are: black body,  $T_{\text{eff}} = 7000$  K,  $\tau_{0.55 \mu\text{m}} = 7.0$ , Draine & Lee (1984) silicates, Mathis et al. (1977) grain size distribution with  $a_{\text{max}} = 0.45 \mu\text{m}$  and  $Y_{\text{out}} = 10^4$ . The symbols refer to the observations (see text) corrected for interstellar extinction of  $A_v = 5^m$ .

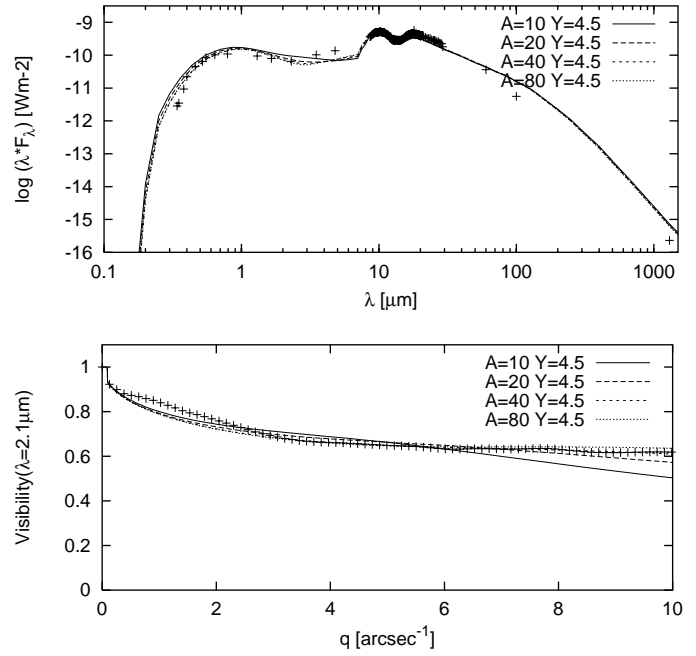


**Fig. 13.** SED (top) and visibility (bottom) for a superwind model with  $Y = r/r_1 = 4.5$  and different amplitudes. The inner shell obeys a  $1/r^2$  density distribution, the outer shell a  $1/r^{1.5}$  density distribution. The temperature at the inner boundary of the hot shell is 1200 K. Model parameters are: black body,  $T_{\text{eff}} = 7000$  K,  $\tau_{0.55 \mu\text{m}} = 7.0$ , Draine & Lee (1984) silicates, Mathis et al. (1977) grain size distribution with  $a_{\text{max}} = 0.45 \mu\text{m}$ , and  $Y_{\text{out}} = 10^4$ . The symbols refer to the observations (see text) corrected for interstellar extinction of  $A_v = 5^m$ .

### 3.4.5. Intensity distributions

Fig. 14 displays the spatial distribution of the obtained normalized model intensity for the model shown in Fig. 10 ( $T_1 = 1000$  K,  $Y = 4.5$ ,  $A = 40$ ,  $1/r^2$  and  $1/r^{1.7}$  density distribution in the inner and outer shell, resp.) The (unresolved) central peak belongs to the central star, and the two local intensity maxima to the loci of the inner rims of the two shells at 35 mas and 157 mas, resp. The  $2.11 \mu\text{m}$  intensity shows a ring-like distribution with a steep decline with increasing distance from the inner boundary of the circumstellar shell. Similarly shaped intensity distributions have also been found by Ivezić & Elitzur (1996) for optically thin shells.

We recall that this intensity distribution is based on radiative transfer models taking into account both the SED and the  $2.11 \mu\text{m}$  visibility. Fig. 15 shows the model visibilities for much higher spatial frequencies than covered by the present observations. The required baselines would correspond to  $\sim 22$  and 440 m instead to 6 m (13.6 cycles/arcsec). Since the dust-shell's diameter is  $\sim 70$  mas a plateau is only reached for spatial frequencies larger than, say, 15 cycles/arcsec depending on the strength of the superwind. The central star is resolved at spatial frequencies of  $\sim 1000$  cycles/arcsec. At frequencies  $\gtrsim 2$  cycles/arcsec the shape of the observed and the modelled visibility function is triangle-shaped, which is a consequence of the ring-like intensity distribution of the dust shell.

Visibility observations are often characterized by fits with Gaussian intensity distributions. The resulting Gaussian FWHM diameter is then assumed to give roughly the typical size of the dust shell. A Gauß fit to the observed visibility would yield a FWHM dust-shell diameter of  $(219 \pm 30)$  mas in agreement with the one given by Christou et al. (1990). However, radiative transfer models show that a ring-like intensity distributions appears to be more appropriate than a Gaussian one for the dust shell of IRC +10 420. The distribution shows a limb-brightened dust condensation zone and a ring diameter of 70 mas.

## 4. Summary

Radiative transfer calculations show that the near-infrared visibility strongly constrains dust shell models since it is, e.g., a sensitive indicator of the grain size. Accordingly, high-resolution interferometry results provide essential ingredients for models of circumstellar dust-shells. Assuming spherical symmetry we carried out radiative transfer calculations for the hypergiant IRC +10 420 to model both its SED and  $2.11 \mu\text{m}$  visibility. Since we failed to find good SED fits for single-component models, we improved our density distribution introducing a second component with enhanced values at a certain distance. For different scaled distances  $Y = r/r_1$  and density enhancements  $A$  of this cool component we considered different grain-size distributions

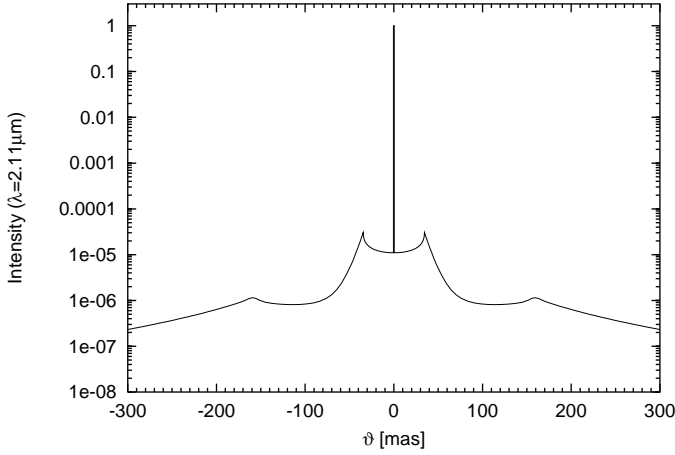


**Fig. 14.** Normalized intensity vs. angular displacement  $\vartheta$  for a superwind model with  $Y = r/r_1 = 4.5$ ,  $A = 40$  and a  $1/r^{1.7}$  density distribution in the outer shell. The (unresolved) central peak belongs to the central star. The inner hot rim of the circumstellar shell has a radius of 35 mas, and the cool component is located at 155 mas. Both loci correspond to local intensity maxima. Model parameters are: black body,  $T_{\text{eff}} = 7000$  K,  $T_1 = 1000$  K,  $\tau_{0.55 \mu\text{m}} = 7.0$ , Draine & Lee (1984) silicates, Mathis et al. (1977) grain size distribution with  $a_{\text{max}} = 0.45 \mu\text{m}$ .

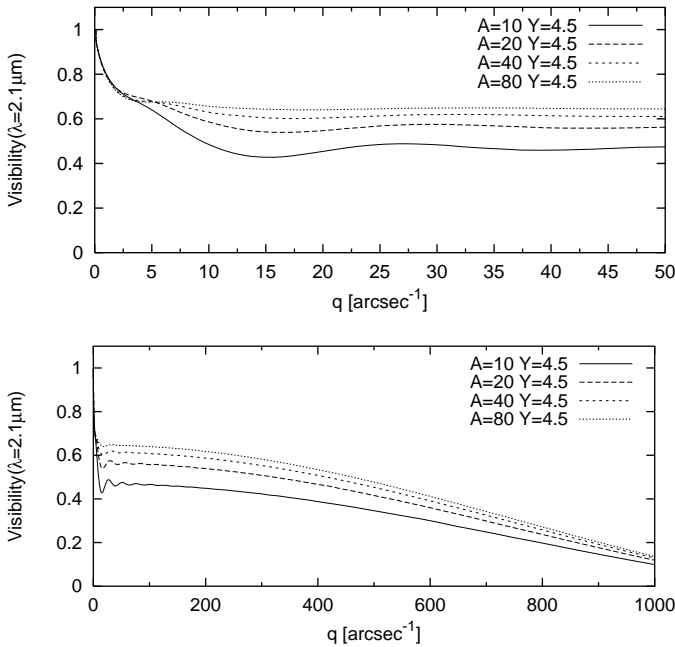


**Fig. 15.** Model visibility up to 50 (top) and 1000 cycles/arcsec (bottom) for a superwind model with  $Y = r/r_1 = 4.5$  and different amplitudes. The inner shell obeys a  $1/r^2$  density distribution, the outer shell a  $1/r^{1.7}$  density distribution. Model parameters are: black body,  $T_{\text{eff}} = 7000$  K,  $T_1 = 1000$  K,  $\tau_{0.55 \mu\text{m}} = 7.0$ , Draine & Lee (1984) silicates, and Mathis et al. (1977) grain size distribution with  $a_{\text{max}} = 0.45 \mu\text{m}$ .

$n(a) \sim a^q$ , density distributions  $\rho \sim 1/r^x$  within the shells, and temperatures  $T_1$  at the inner boundary of the hot shell.

An MRN grain size distribution  $n(a) \sim a^{-3.5}$  with  $0.005 \mu\text{m} \leq a \leq 0.45 \mu\text{m}$  was found to be well suited for

IRC +10 420. Larger negative exponents, i.e. a narrower distribution, can be accounted for by increasing the maximum grain size. For instance,  $n(a) \sim a^{-3.8}$  requires  $a_{\text{max}} \sim 0.55 \mu\text{m}$ . However, the range of appropriate exponents seemed to be quite small and steeper declining distributions led to significantly worse fits.

Assuming a  $1/r^2$  density distribution for both shells and  $T_1 = 1000$  K gives the best fit for  $Y = 4.5$  and  $A = 40$  (Fig. 6). This model can be improved by introducing a somewhat flatter density distribution, viz.  $\sim 1/r^{1.7}$ , for the outer shell leading to a better match with the observed SED for  $\lambda \gtrsim 20 \mu\text{m}$ . The quality of the visibility fit remains almost unchanged (Fig. 10). Both models show a somewhat larger curvature of the visibility at low spatial frequencies. However, the deviations are within the observational uncertainties. The various flux contributions at  $2.11 \mu\text{m}$  are 62.2% stellar light, 26.1% scattered radiation and 10.7% dust emission.

Alternatively one may increase the temperature at the inner boundary of the hot shell to  $T_1 = 1200$  K which gives somewhat better matches to the near-infrared flux and lowers the low-frequency visibility curvature. To counteract the concomitant loss of flux in the far-infrared one has to assume a  $1/r^{1.5}$  density distribution (Fig. 13). The fit to the silicate features is, however, somewhat worse than in the case of the  $T_1 = 1000$  K model.

The intensity distribution was found to be ring-like. This appears to be typical for optically thin shells (here  $\tau_{0.55 \mu\text{m}} = 7$ ,  $\tau_{2.11 \mu\text{m}} = 0.55$ ; see also Ivezić & Elitzur 1996) showing limb-brightened dust-condensation zones. Accordingly, the interpretation of the observational data by FWHM Gauß diameters may give misleading results.

The two components can be interpreted as if IRC +10 420 has suffered from much higher mass-loss rates in its recent past than today. For instance, the  $T_1 = 1000$  K model gives  $\dot{M}_1 = 1.4 \cdot 10^{-5} M_{\odot}/\text{yr} \cdot (d/\text{kpc})$  and  $\dot{M}_2 = 8.5 \cdot 10^{-4} M_{\odot}/\text{yr} \cdot (d/\text{kpc})$ . The kinematic age of the outer component gives a corresponding timescale of  $\sim 100$  yr (for  $d = 5$  kpc). If  $T_2 = 1200$  K both shells are located closer to the central star by approximately 30% leading to a correspondingly smaller timescale. The failure of constant mass-loss wind models to fit the SED agrees with the findings of Oudmaijer et al. (1996) and Humphreys et al. (1997). A previous high mass-loss episode is in line with the suspected post-RSG stage of IRC +10 420.

Although, the present observations give only marginal evidence for deviation from spherical symmetry (if elliptical, position angle of the long axis  $\sim 130^\circ \pm 20^\circ$ , axis ratio  $\sim 1.0$  to 1.1), the hot shell may also be interpreted as a disk with a typical diameter of approximately 50 mas. The presence of a rotating equatorial disk has been proposed by Jones et al. (1993), and Oudmaijer et al. (1996) interpreted their hot dust-shell as a disk as well. Provided the disk is not viewed pole-on, the corresponding two-dimensional power spectra should be clearly elongated. It should be noted, however, that disks with an extension of typically 50 mas can only be detected in the power spectra if they provide at least, say, 10% of the total flux. Oudmaijer (1995) discussed several models for the circumstellar shell of IRC +10 420 and found neither a bipolar nor a disk-like wind to be consis-

tent with optical and infrared high-resolution spectroscopy. This seems to be supported by the present observations. In order to be in line with optical blue-shifted emission lines and red-shifted absorption lines Oudmaijer suggested the scenario of infall of circumstellar material onto the stellar photosphere. However, according to Klochkova et al. (1997) the concept of accretion does not appear to be unproblematic either.

Thus, the question which scenario is best suited still appears to be a matter of debate. Bispectrum speckle interferometry gives important information on the spatial extension of the circumstellar shell. It will be in particular the combination of different observations - photometry, spectroscopy and high-resolution imaging - and their simultaneous modelling, which will shed more light on the nature of IRC +10420 that is probably being witnessed in its transition to the Wolf-Rayet phase.

*Acknowledgements.* The observations were made with the SAO 6 m telescope operated by the Special Astrophysical Observatory, Russia. We thank R. Oudmaijer for valuable discussions on this outstanding object and M.A.T. Groenewegen for providing us with the '1992' data set of the SED. The radiative-transfer calculations are based on the code DUSTY developed by Ž. Ivezić, M. Nenkova and M. Elitzur. A. Gauger and A. Men'shchikov are thanked for various discussions on radiative transfer problems. We are grateful to the referee for instructive remarks.

## References

- Bowers P.F., 1984, ApJ 279, 350  
 Bowers P.F., Knapp G.R., 1989, ApJ 347, 325  
 Christou J.C., Ridgway S.T., Buscher D.F., Haniff C.A., McCarthy Jr. D.W., 1990, In: Elston R. (ed.) *Astrophysics with infrared arrays*. ASP conf. series 14, p. 133  
 Cobb M.L., Fix J.D., 1987, ApJ 315, 325  
 Craine E.R., Schuster W.J., Tapia S., Vrba F.J., 1976, ApJ 205, 802  
 David P., Pegourie B., 1995, A&A 293, 833  
 Diamond P.J., Norris R.P., Booth R.S., 1983, A&A 124, L4  
 Draine B.T., Lee H.M., 1984, ApJ 285, 89  
 Dyck H., Zuckerman B., Leinert C., Beckwith S., 1984, ApJ 287, 801  
 Fix J.D., Cobb M.L., 1987, ApJ 312, 290  
 García-Segura G., Langer N., Mac Low M.-M., 1996, A&A 316, 133  
 Gauger A., Balega Y., Irrgang P., Osterbart R., Weigelt G., 1999, A&A 346, 505  
 Giguere P.T., Woolf N.J., Webber J.C., 1976, ApJ 207, L195  
 Groenewegen M.A.T., 1997, A&A 317, 503  
 Hanson M.M., Conti P.S., Rieke M.J., 1996, ApJS 107, 281  
 Hofmann K.-H., Weigelt G., 1986, A&A 167, L15  
 Humphreys R.M., Smith N., Davidson K., et al., 1997, AJ 114, 2778  
 Humphreys R.M., Strecker D.W., Murdock T.L., Low F.J., 1973, ApJ 179, L49  
 Hrivnak B.J., Kwok S., Volk K.M., 1989, ApJ 346, 265  
 Ivezić Ž., Elitzur M., 1996, MNRAS 279, 1019  
 Ivezić Ž., Elitzur M., 1997, MNRAS 287, 799  
 Ivezić Ž., Nenkova M., Elitzur M., 1997, User Manual for DUSTY, University of Kentucky (<http://www.pa.uky.edu/~moshe/dusty>)  
 Jones T.J., Humphreys R.M., Gehrz R.D., et al., 1993, ApJ 411, 323  
 Kastner J., Weintraub D.A., 1995, ApJ 452, 833  
 Klochkova V.G., Chentsov E.L., Panchuk V.E., 1997, MNRAS 292, 19  
 Knapp G.R., Morris M., 1985, ApJ 292, 640  
 Krüger D., Sedlmayr E., 1997, A&A 321, 557  
 Kurucz R.L., 1992, In: Barbuy B., Renzini A. (eds.) *The Stellar Populations of Galaxies*. IAU Symp. 149, Kluwer, Dordrecht, p. 225  
 Labeyrie A., 1970, A&A 6, 85  
 Lohmann A.W., Weigelt G., Wirtitzer B., 1983, Appl. Opt. 22, 4028  
 Mathis J.S., Rumpl W., Nordsieck K.H., 1977, ApJ 217, 425 (MRN)  
 McLaren R.A., Betz A.L., 1980, ApJ 240, L159  
 Menten K.M., Alcolea J., 1995, ApJ 448, 416  
 Mutel R.L., Fix J.D., Benson J.M., Webber J.C., 1979, ApJ 228, 771  
 Nedoluha G.E., Bowers P.F., 1992, ApJ 392, 249  
 Oudmaijer R.D., 1995, Ph.D. Thesis, University of Groningen  
 Oudmaijer R.D., 1998, A&AS 129, 541  
 Oudmaijer R.D., Geballe T.R., Waters L.B.F.M., Sahu K.C., 1994, A&A 281, L33  
 Oudmaijer R.D., Groenewegen M.A.T., Matthews H.E., Blommaert J.A.D.L., Sahu K.C., 1996, MNRAS 280, 1062  
 Ossenkopf V., Henning T., Mathis J.S., 1992, A&A 261, 567  
 Ridgway S.T., Joyce R.R., Connors D., Pipher J.L., Dainty C., 1986, ApJ 302, 662  
 Savage B.D., Mathis J.S., 1979, ARA&A 17, 73  
 Schaller G., Schaerer D., Meynet G., Maeder A., 1992, A&AS 96, 269  
 Suh K.W., Jones T.J., 1997, ApJ 479, 918  
 Walmsley C.M., Chini R., Kreysa E., et al., 1991, A&A 248, 555  
 Weigelt G., 1977, Optics Commun. 21, 55  
 Winters J.M., Fleischer A.J., Le Bertre T., Sedlmayr E., 1997, A&A 326, 305